



TECHNICAL ARTICLE

Enhanced Mechanical Properties and Corrosion Resistance by Minor Gd Alloying with a Hot-Extruded Mg Alloy

Huai Yao, Shubo Wang, Yi Xiong, Xinying Shi, Harishchandra Singh, Marko Huttula, and Wei Cao

Submitted: 16 February 2022 / Revised: 13 April 2022 / Accepted: 14 April 2022 / Published online: 26 May 2022

The microstructure, mechanical properties, and corrosion resistance to simulated body fluid solution behavior of as-extruded Mg-1.8Zn-0.5Zr alloys with different Gd additions are investigated. It is found that dynamic recrystallization occurs in the alloys during extrusion and the grain size gradually decreases with Gd alloying. The mechanical properties and corrosion resistance to simulated body fluid of the investigated alloys enhance firstly and then weaken with the increase in Gd content. The results reveal that the Mg-1.8Zn-0.5Zr with a 1.5 wt.% Gd addition has optimized mechanical properties and corrosion resistance. A three-stage corrosion mechanism, including sequential stages from hydroxidation, phosphatization and hydroxidation, to formation-dissolution dynamic equilibrium, is proposed through electrochemical measurements and corroded surface analyses. This study reveals the extruded Mg-1.8Zn-0.5Zr-1.5Gd alloy can be regarded as a potential candidate for using as biodegradable magnesium implants.

Keywords biodegradation, corrosion, magnesium alloys, mechanical properties, microstructure

1. Introduction

Magnesium (Mg) alloys have attracted considerable attentions as biodegradable implant materials due to their outstanding biocompatibility and biodegradation together with efficient mechanical properties (Ref 1, 2). In general, biodegradable implant Mg alloys should have a yield strength (YS) greater than 200 MPa, elongation higher than 10%, and corrosion rate lower than 0.5 mm/y (Ref 3). However, some drawbacks, including rapid corrosion rate due to localized corrosion and relatively low strength compared with stainless steels and Ti alloys, have limited their extensive clinical applications (Ref 4).

Huai Yao, School of Materials Science and Engineering, Henan University of Science and Technology, Luoyang 471023 Henan, China; and Provincial and Ministerial Co-construction of Collaborative Innovation Center for Non-ferrous Metal New Materials and Advanced Processing Technology, Luoyang 471023 Henan, China; **Shubo Wang**, **Harishchandra Singh**, and **Wei Cao**, Nano and Molecular Systems Research Unit, Centre for Advanced Steels Research, University of Oulu, FI-90014 Oulu, Finland; **Yi Xiong**, School of Materials Science and Engineering, Henan University of Science and Technology, Luoyang 471023 Henan, China; **Xinying Shi**, School of Physics and Electronic Engineering, Jiangsu Normal University, Xuzhou 221116 Jiangsu, China; **Marko Huttula**, School of Materials Science and Engineering, Henan University of Science and Technology, Luoyang 471023 Henan, China; and Nano and Molecular Systems Research Unit, Centre for Advanced Steels Research, University of Oulu, FI-90014 Oulu, Finland. Contact e-mail: yaohuaitougao@126.com.

Alloying and microstructure manipulation are feasible approaches to improve the mechanical properties and corrosion resistance of Mg alloys. Zn and Zr have been selected as they are nutrient elements to the human body (Ref 5). A small amount of Zn (~2.0wt.%) is believed to form a protective film on the surface of the Mg alloy, which improves its corrosion resistance (Ref 6). Alloying with Zr, a useful grain refinement element, can also improve the mechanical properties and corrosion resistance of Mg alloy (Ref 7). Recent researchers have found that the addition of RE (rare earth) elements in Mg-Zn-Zr-based alloys enhances the mechanical properties and corrosion resistance (Ref 8-10). Meanwhile, thermal mechanical deformations, such as hot extrusion and rolling, are also used to achieve enhanced mechanical properties in these alloys (Ref 11-13). For example, high ultimate tensile strength (UTS) of 285 MPa, YS of 200 MPa and elongation to failure (EL) of 23% were achieved in Mg-1Zn-0.4Zr-8Gd alloy after hot extrusion compared with the as-cast one (Ref 14). Hot extrusion of as-cast Mg-0.22Zn-0.44Zr-3.09Nd alloy led to an increase in UTS to 307 MPa, YS to 293 MPa and EL to 15.9% (Ref 15). Additionally, the as-cast Mg-2.0Zn-0.5Zr-3.0Gd alloy exhibited a corrosion rate of less than 0.5 mm/y after hot extrusion (Ref 16). Nevertheless, the inhomogeneous distribution of secondary phases due to the addition of alloying elements in as-extruded Mg alloy can lead to severe localized corrosion (Ref 17). Wang et al. reported that a homogenization treatment of Mg-Zn-Zr-Y alloy could help to overcome this shortcoming (Ref 18). An Mg-2.4Zn-0.8Gd alloy with a prior solid solution treatment before extrusion showed an improved corrosion resistance compared with the one without solution treatment. Such improvements were ascribed to the more uniform grain structure and dispersed secondary phases (Ref 19). Despite the improvements in mechanical properties and corrosion resistance, most of the aforementioned RE elements are hepatotoxic and hazardous to a person's health. Recent studies on Gd containing Mg alloys show that the Gd released

by the alloy during degradation is harmless to the human body and has a certain anti-cancer effect when the Gd content is less than 2.5 wt.% (Ref 20-22).

Considering biosafety, the Gd content in such biodegradable Mg alloy should be low. To date, a very few works have been done on the effects of minor Gd alloying on the microstructures, mechanical properties and corrosion behavior of as-extruded Mg-Zn-Zr-based alloys, especially on those with prior solid solution treatment. Herein, in this paper, Mg-1.8Zn-0.5Zr-xGd ($x = 0, 0.5, 1.0, 1.5, 2.0, 2.5$ wt.%) alloys were prepared by solid solution treatment and hot extrusion. The effects of small amounts of Gd on the microstructural evolution, mechanical properties and corrosion resistance in simulated body fluid (SBF) solution of extruded Mg-1.8Zn-0.5Zr alloys were investigated systematically, to optimize the composition of Mg-Zn-Zr alloys that can be used as biodegradable materials. It is hoped that our research will benefit the general bioimplant material designs beyond the invention of Mg alloys and their engineering design strategies.

2. Experimental Materials and Methods

2.1 Experimental Materials

Mg-1.8Zn-0.5Zr-xGd alloys were prepared by melting Mg (99.9%), Zn (99.9%), and Mg-30Zr (wt.%) and Mg-20Gd (wt.%) master alloys in an electric induction furnace and then casting (Ref 23). Afterward, the cast ingots were machined into cylindrical bars with a diameter of 50 mm and a height of 35 mm. The as-cast bars were solution-treated at 480 °C for 6 h and then extruded at 360 °C with an extrusion speed of 5 mm/s and an extrusion ratio of 7.7 to a diameter of 18 mm. All the extruded rods were then subjected to stress relief annealing at 200 °C for 4 h. Hereafter, these as-extruded Mg-1.8Zn-0.5Zr-xGd ($x=0, 0.5, 1.0, 1.5, 2.0, 2.5$ wt.%) alloys were donated as $E_s0, E_s0.5, E_s1.0, E_s1.5, E_s2.0$ and $E_s2.5$, respectively.

2.2 Microstructure and Mechanical Property Determination

The specimens for microstructure observation were cut from the central region, parallel to the extrusion direction (ED) of the extruded rods. Microstructure characterizations were performed by an optical microscope (OLYMPUS, PMG3), a scanning electron microscope (SEM, JSM-7800F) equipped with energy-dispersive x-ray spectrometer (EDS) and a transmission electron microscope (TEM, JEM-2100). Sample preparation was carried out the same way as those described in our previous work (Ref 24). Tensile specimens were machined from extruded rods parallel to the ED with a gauge length of 25 mm and a gauge diameter of 5 mm. According to the ASTM E8M-09 standard, tensile tests were performed at a speed of 1 mm/min using an AG-1250KN (SHIMADZU) machine.

2.3 Corrosion Tests

The corrosion rate of these selected alloys was evaluated by measuring the weight loss during immersion test in SBF solution (Ref 25) at 37 °C. The samples with a dimension of $\Phi 18 \times 5$ mm were immersed in 180 mL SBF. The SBF solution was refilled every 8 h to keep a constant pH value. After the immersion test, the corrosion products were removed using a

200 g/L $\text{CrO}_3 + 10$ g/L AgNO_3 solution. The average corrosion rate was calculated using the following equation (Ref 26):

$$P_w = 8.76 \times 10^4 \times \Delta w / A t \rho \quad (\text{Eq 1})$$

where P_w is the corrosion rate (mm/y), Δw is the mass loss (g), A is the specimen surface area exposed to the SBF solution (cm^2), t is the immersion time (h), and ρ is the density of the alloy (g/cm^3), respectively.

For electrochemical test, cylindrical samples were mounted into epoxy resin with a surface area of 1 cm^2 exposed to the SBF solution. Potentiodynamic polarization curve and electrochemical impedance spectroscopy (EIS) measurements were carried out at 37 °C using an electrochemical workstation (Autolab PGSTAT128N) to reveal the corrosion behavior of Mg-1.8Zn-0.5Zr-xGd alloys. The chosen alloys, a saturated calomel electrode and graphite sheet were used as working, reference and counter electrode, respectively. Prior to the electrochemical tests, the samples were soaked in the SBF solution for 1 h to achieve equilibrium. The polarization curves were acquired by scanning from -0.25 to $+0.4$ V versus the open-circuit potential (OCP) at a scan rate of 1 mV/s. The EIS measurements were carried out at OCP using an AC amplitude of 10 mV in the frequency range from 10 kHz to 0.1 Hz.

X-ray photoelectron spectroscopy (XPS) was used to analyze the chemical composition of corrosion products formed on the surface of $E_s1.5$ alloy after SBF immersion for 16, 48, and 120 h. XPS measurements were taken on a Thermo Fisher Scientific ESCALAB 250Xi XPS spectrophotometer. The core-level 1s peak of the adventitious carbon is employed for the overall energy calibration. Mg 1s and Ca 2p spectra were measured and fitted.

3. Results

3.1 Microstructure Evolution

Figure 1 shows the optical images of the as-extruded Mg-1.8Zn-0.5Zr-xGd alloys. The near-equiaxed uniform grain structures of E_s0 shown in Fig. 1(a) indicate the occurrence of complete dynamic recrystallization (DRX) during hot extrusion. The average grain size of E_s0 is measured to be about $17.9 \mu\text{m}$. With the addition of Gd, one can see a bimodal grain structure in the alloys: relatively coarse grains and band-shaped fine-grain regions (highlighted in Fig. 1d) distributed along with ED. Average grain sizes of these alloys are estimated to be about 9.6, 7.5, 7.3, 7.2, and $6.8 \mu\text{m}$ from 0.5 to 2.5 wt.% Gd, respectively. More second-phase particles are found to distribute along ED in the alloys with high Gd content (2.0, 2.5 wt.%).

Figure 2 gives the TEM characterization results of $E_s1.5$ alloy. Figure 2(a) reveals the presence of subgrains and a small amount of nanoscale second-phase particles that disperse mainly along the DRXed (sub)grain boundaries. The selected area electron diffraction (SAED) pattern of particle (marked as A) reveals that the particles have a face-centered cubic crystal structure. Interplanar spacings are 0.4219, 0.2197, and 0.2581 nm, which can be indexed to the $(1 \bar{1} \bar{1})$, $(31 \bar{1})$ and (220) planes of Mg_3Gd phase. EDS spectrum in Fig. 2(b) shows that the particles are composed of Mg, Zn and Gd, suggesting a $(\text{Mg}, \text{Zn})_3\text{Gd}$ phase with Zn dissolved in Mg_3Gd . This finding is in agreement with other Zn and Gd containing Mg alloys (Ref 27).

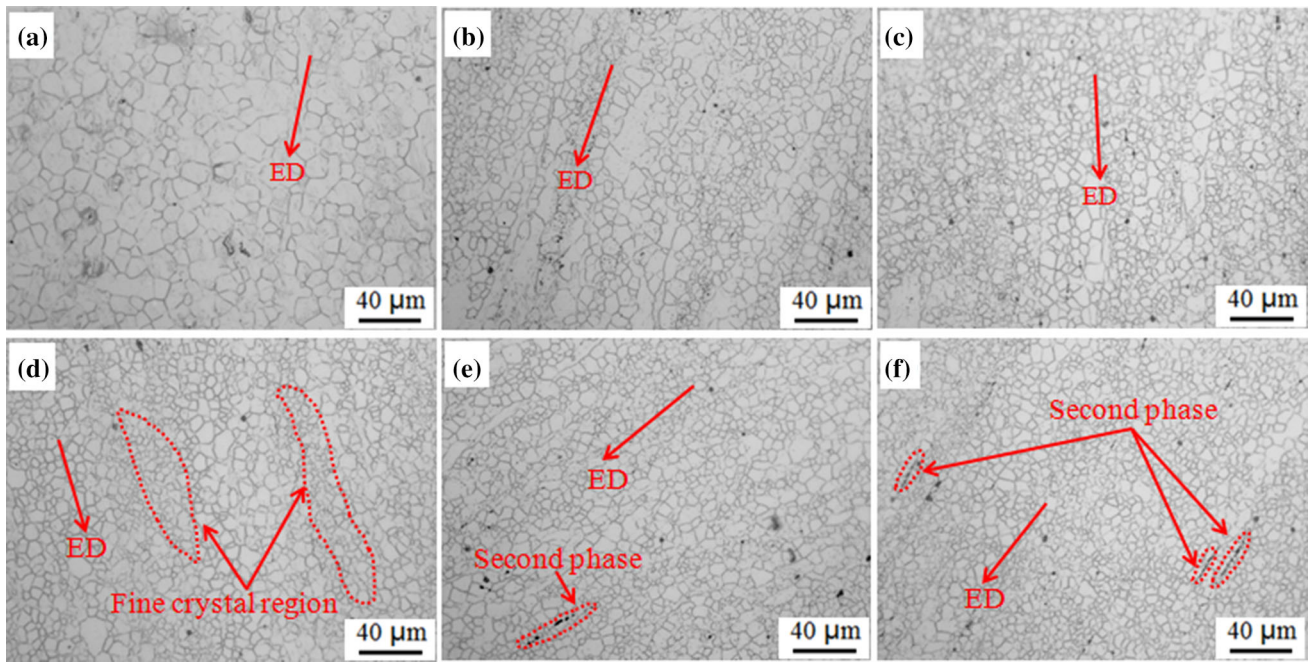


Fig. 1 Optical micrographs of the as-extruded alloys: (a) E_s0 , (b) $E_s0.5$, (c) $E_s1.0$, (d) $E_s1.5$, (e) $E_s2.0$, (f) $E_s2.5$ alloy, respectively

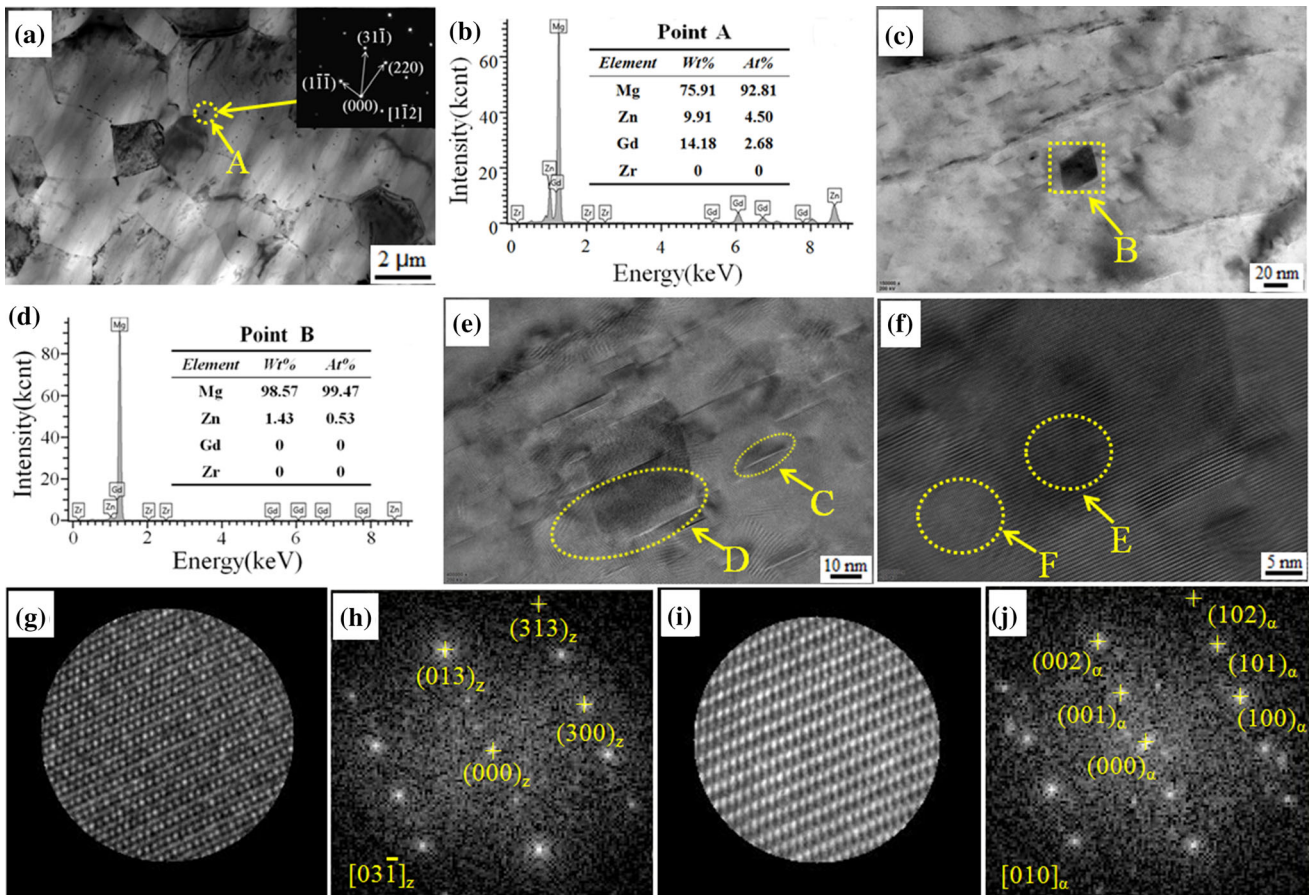


Fig. 2 TEM characterizations of second-phase particles in the $E_s1.5$ alloy. (a) BF-TEM image, (b) EDS spectrum of particle A; (c) BF-TEM image of rectangular shaped particles, (d) EDS spectrum of particle B; (e) enlarged image of B in (c); (f) HR-TEM image of D in (e); (g) HR-TEM image of the nanoscale second-phase particle and (h) its FFT image; (i) HR-TEM image and (j) its FFT image of the α -Mg matrix. The inset of (a) shows the SAED of particle A

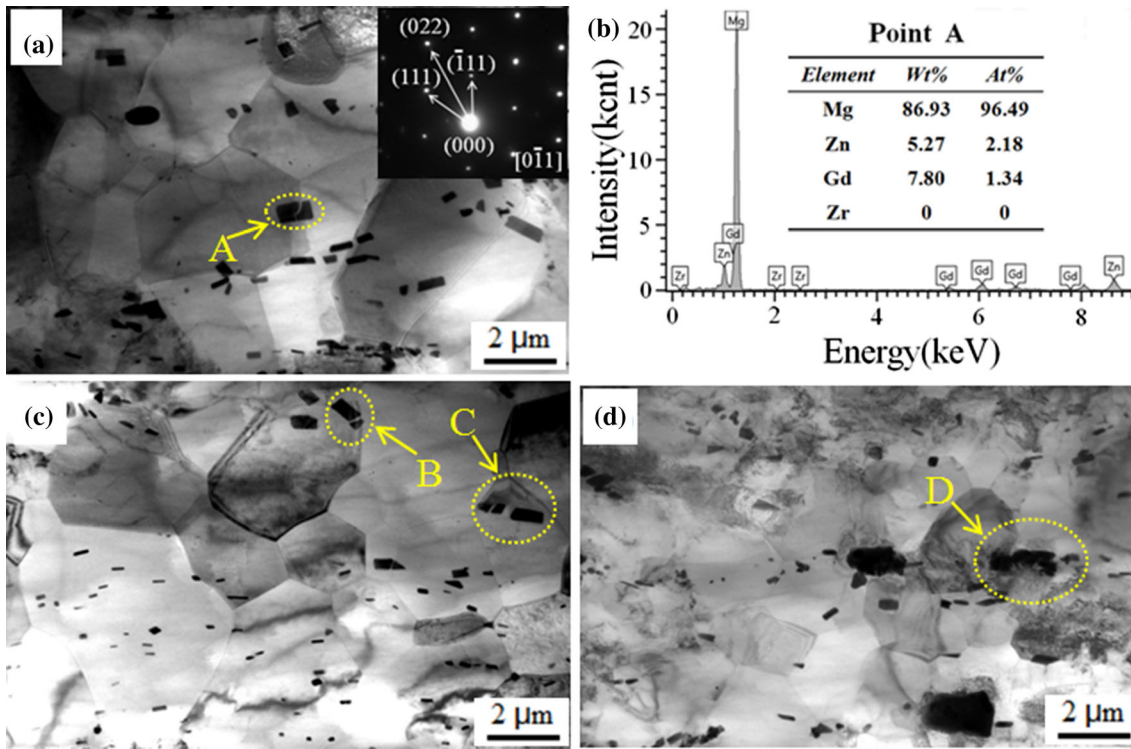


Fig. 3 TEM characterization of second-phase particles in $E_32.5$ alloy: (a, c, d) BF-TEM images, and (b) EDS spectrum of particle A. The inset of (a) shows the SAED of particle A

Second-phase particles with a rectangular-shaped cross section are also found in the Mg matrix (Fig. 2c). EDS spectrum in Fig. 2(d) shows that the particles (marked as B) are composed of Mg and Zn. It should be noted that from the magnified image of B in Fig. 2(c), there are also some lath-shaped fine structures, e.g., in region C, showing a relatively weak contrast to the Mg matrix. HR-TEM image in Fig. 2(f), magnification of region D in Fig. 2(e), shows a distorted lattice implying the segregation of alloying elements with a different lattice constant other than Mg. These laths might be the nucleation sites of the second-phase precipitates (Ref 28). Fourier transform (FFT) is performed on the second-phase particle (E) and α -Mg matrix (F) in Fig. 2(f). The second-phase particle (E) is detected to have a primitive cube crystal structure from the FFT of the HRTEM image (Fig. 2g, and h). The interplanar spacings of 0.2711, 0.1969 and 0.2857 nm have a good correspondence with those of $(013)_z$, $(313)_z$ and $(300)_z$ planes of Mg_2Zn_{11} phase with $[0.3\bar{1}]_z$ zone axis parallel to the electron beam. Considering the chemical compositions in Fig. 2(d), it can be concluded that the particle is Mg_2Zn_{11} . Figures 2(i) and (j) show the HRTEM and FFT image of Mg matrix adjacent to the Mg_2Zn_{11} particle (region F), respectively. It is found that the $[010]_\alpha$ zone axis of hcp Mg is parallel to the electron beam. Accordingly, the results demonstrate that the orientation relationship between nanoscale Mg_2Zn_{11} phase and Mg matrix is $(013)_z \parallel (002)_\alpha$, $(313)_z \parallel (102)_\alpha$ and $(300)_z \parallel (100)_\alpha$. The lattice mismatch (δ) of phase interface can be calculated by (Ref 29):

$$\delta = 2(X_A - X_B)/(X_A + X_B) \quad (\text{Eq 2})$$

where X_A and X_B are the interplanar distance of corresponding parallel plane pairs. The calculation results in the lattice mismatch of $(013)_z \parallel (002)_\alpha$, $(313)_z \parallel (102)_\alpha$, and $(300)_z \parallel (100)_\alpha$

are 0.039, 0.035 and 0.027, respectively, implying that the nanosized Mg_2Zn_{11} particles have a coherent interfacial relationship with the neighboring α -Mg matrix.

Figure 3 shows the TEM characterization of the second-phase particles in $E_32.5$ alloy. In contrast to the nanoscale particles in the $E_31.5$ alloy, the particles in Fig. 3(a) with a size of larger than $1 \mu\text{m}$, clearly, are much coarser and aligned as 'dashed line'. EDS analysis (Fig. 3b) on the particles (marked as A) indicates that the second-phase particles are mainly composed of three elements: Mg, Zn and Gd. SAED of the particle infers that the particle is similar to the second-phase particle in Fig. 2(a) and belongs to the $(Mg, Zn)_3Gd$ phase. More BF-TEM images (Fig. 3c and d) reveal the existence of broken $(Mg, Zn)_3Gd$ particles (marked as B, C and D). Accordingly, it can be concluded that some $(Mg, Zn)_3Gd$ -based particles have not dissolved into the alloy matrix during solid solution treatment and been crushed to smaller pieces during extrusion process.

3.2 Mechanical Properties and Fracture Surfaces

The engineering stress-strain curves of as-extruded Mg-1.8Zn-0.5Zr-xGd alloys are plotted in Fig. 4. The UTS, YS, and EL values are summarized in Table 1. Impressively, alloying Gd with the Mg-Zn-Zr alloy significantly improves the strength and ductility. The alloy with 2.0 wt.% Gd has the best mechanical properties, and its UTS, YS, and EL values are 288.5 ± 3.0 MPa, 257.6 ± 2.8 MPa and $33.5 \pm 1.2\%$.

Figure 5 shows the fracture surfaces of the extruded Mg-1.8Zn-0.5Zr-xGd alloys after tensile failure. Without Gd, fracture surface of the alloy is characterized of quasi-cleavage fracture together with fine but shallow dimples decorating the surface (Fig. 5a). With increasing Gd content to 2.0 wt.%, the

size and number of dimples gradually increase, while the quasi-cleavage fractures gradually decrease until they disappear, shifting to more ductile fractures. Second-phase particles with a size of about 1 μm are found in the fracture surface of $E_s2.0$ alloy, as marked by the yellow ellipses in Fig. 5(e). When the Gd content increases to 2.5 wt.% (Fig. 5f), the size of second-phase particles seen in the fracture surface is about 2.5 μm .

3.3 Corrosion Behavior

Figure 6(a) shows the polarization curve of the as-extruded Mg-1.8Zn-0.5Zr-xGd alloys measured after 1 h of immersion in SBF solution. Table 2 summaries the self-corrosion potential (E_{corr}), self-corrosion current density (I_{corr}) and corrosion rate (P_i) obtained by Tafel extrapolation. In general, alloying Gd with the Mg alloys has a considerable enhancement of the corrosion resistance, evidenced by the more positive E_{corr} , lower I_{corr} and P_i . The alloy with 1.5 wt.% Gd owns the lowest P_i . After 120 h of immersion (Fig. 6b), the alloy with 1.5 wt.% Gd still possesses the lowest P_w estimated by average weight loss. The $E_s1.5$ alloy could be a promising medical implanting alternative with excellent mechanical properties, corrosion resistance and high biosafety (only 1.5 wt.% RE content).

To study the corrosion resistance of $E_s1.5$ alloy, EIS spectra (Nyquist plots, impedance modulus and phase angle of Bode plots) from the $E_s1.5$ alloy after different immersion times in SBF were analyzed, as presented in Fig. 7. Two capacitive loops in high frequency and medium/low frequency are shown in the Nyquist plots. Nevertheless, the loops have different radii. The medium to low-frequency capacitive loop band is usually related to the charge transfer resistance of corrosion

layer, while the high-frequency capacitive loop is usually related to the charge transfer resistance of oxide film on the alloy surface (Ref 30). As is known, the larger the radius of the capacitive loop, the stronger the corrosion resistance of the alloy in the solution (Ref 31). The radius of the high-frequency loop increases with longer immersion times, implying decreased corrosion rate of the alloy with increasing immersion time. Additionally, Fig. 7(d) shows the equivalent circuit model for fitting of the EIS plots, in which R_s stands for electrolyte resistance between the reference and working electrode, R_1 and CPE_1 are the resistance of Mg^{2+} through the corrosion layer and double-layer capacitance of the corrosion layer/electrolyte interface. R_2 and CPE_2 are the resistances of MgO barrier film and the double-layer capacitance of substrate/MgO film, respectively. Due to non-uniform current and potential distributions, constant phase element (CPE) is employed here to study a non-ideal capacitor deviated from the ideal capacitive behavior at the interfaces (Ref 32). The extracted data are summarized in Table 3. R_s has a value about 15~30 Ω in the SBF solution. A rapid increase in R_1 and R_2 can be observed in the first 48 h, corresponding to an increase resistance of the corrosion product layer over time. The R_1 and R_2 increase slowly from 48 to 96 h, which can be related to the increase thickness of the corrosion product layer. After 96 h, the R_1 and R_2 tend to be stable with prolonged immersion time. This is attributed to the near-dynamic equilibrium of dissolution and generation of corrosion products after renewal of the SBF solution (Ref 33).

Figure 8 shows the P_w of the $E_s1.5$ alloy every 8 h after immersed in SBF solution for 120 h. The P_w decreases rapidly with increasing immersion time within 48 h firstly, then decreases gradually, and finally achieves a plateau after 96 h of immersion, showing a good agreement with the results in Fig. 7 and Table 3.

The corrosion morphologies of the $E_s1.5$ alloy after immersion for 16, 32, 48 and 120 h were characterized by SEM and are shown in Fig. 9. Corresponding macroscopic images after the removal of corrosion products are also shown as the inset images. After 16 h of immersion (inset of Fig. 9a), the alloy surface is relatively uniform and shows no trace of local corrosion. With increasing immersion time, line-like corrosion areas began to appear (inset of Fig. 9b) and then became wider (inset of Fig. 9c). The area with corrosion products increases until the corrosion products covers the entire alloy surface after 120 h of immersion (inset of Fig. 9d). Meanwhile, the thickness of corrosion product layer and the width of cracks forming in the corrosion layer increase gradually. The as-observed cracks are mainly caused by the dehydration in the water-containing corrosion layer during drying (Ref 34). As shown in Table 4, when the immersion time is 16 and 32 h, EDS results of the corrosion products (A and B areas) of the investigated alloys show that the corrosion

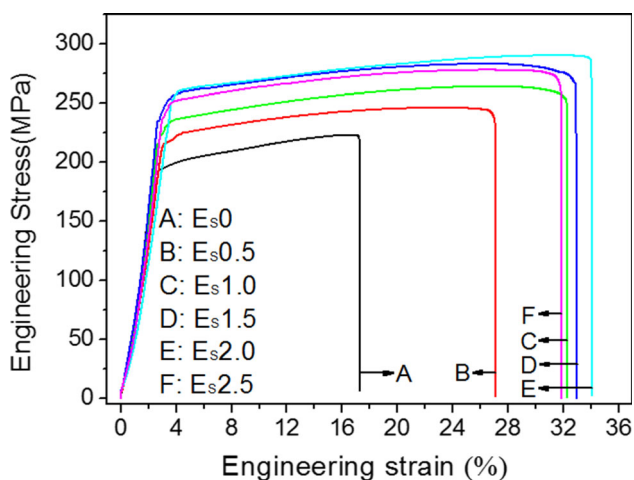


Fig. 4 Engineering stress–strain curves of as-extruded Mg-1.8Zn-0.5Zr-xGd alloys

Table 1 Mechanical properties of as-extruded Mg-1.8Zn-0.5Zr-xGd alloys

Material	E_s0	$E_s0.5$	$E_s1.0$	$E_s1.5$	$E_s2.0$	$E_s2.5$
UTS, MPa	228.4 ± 2.7	244.3 ± 2.8	262.6 ± 3.1	280.8 ± 2.9	288.5 ± 3.0	276.7 ± 2.9
YS, MPa	192.8 ± 2.5	217.7 ± 2.6	233.2 ± 2.8	252.4 ± 2.7	257.6 ± 2.8	248.6 ± 2.7
EL, %	17.2 ± 0.9	26.7 ± 1.2	32.1 ± 1.1	32.9 ± 1.3	33.5 ± 1.2	31.5 ± 1.3

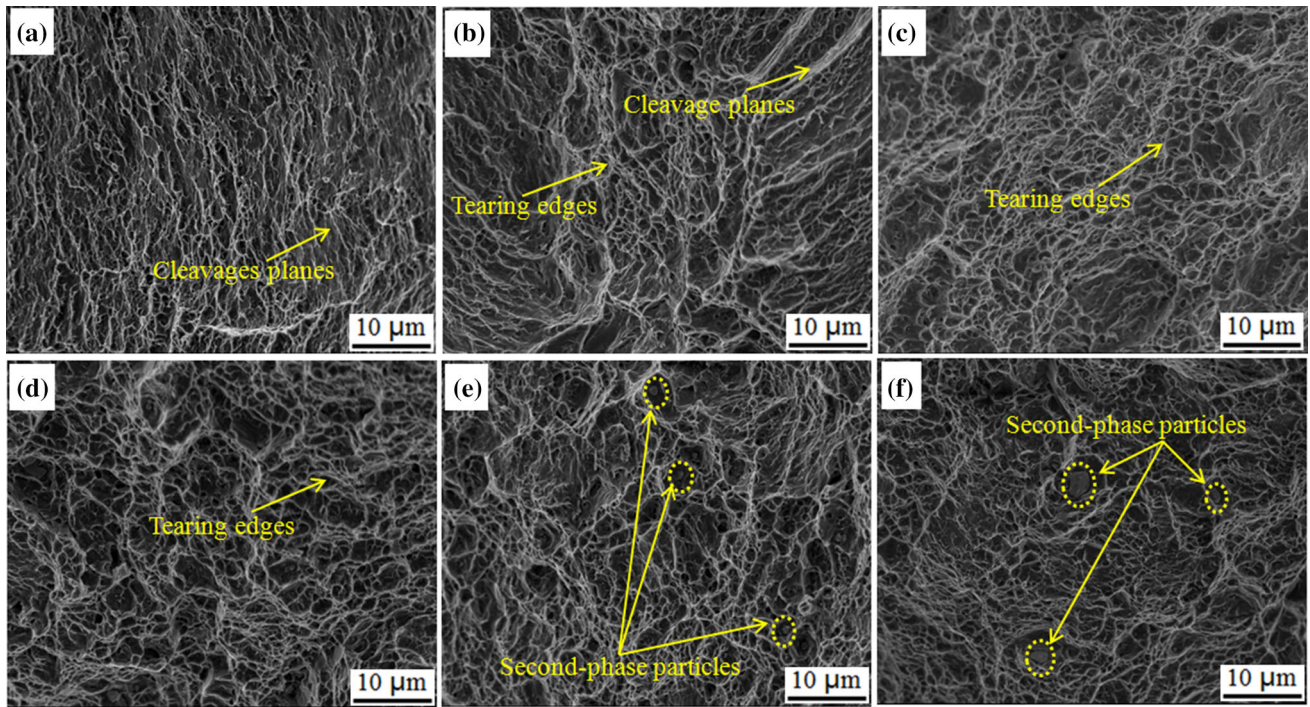


Fig. 5 Fracture surfaces of as-extruded (a) E_s0 ; (b) $E_s0.5$; (c) $E_s1.0$; (d) $E_s1.5$; (e) $E_s2.0$; (f) $E_s2.5$ alloy

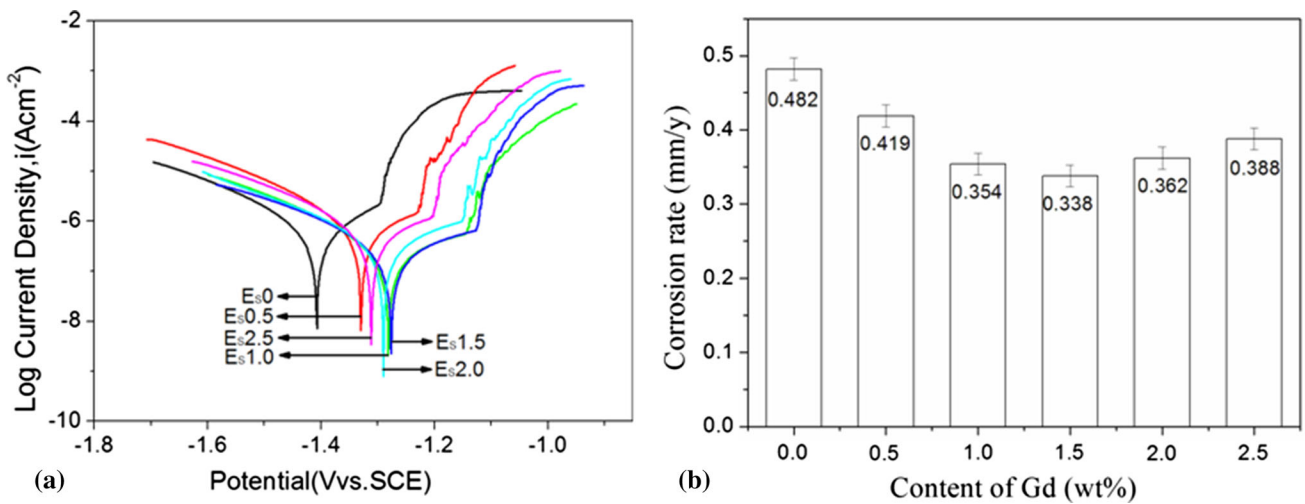


Fig. 6 (a) Polarization curves of as-extruded Mg-1.8Zn-0.5Zr-xGd alloys measured after 1 h of immersion in SBF solution, and (b) P_w calculated by weight loss after 120 h of immersion in SBF solution

Table 2 E_{corr} , I_{corr} and P_i of as-extruded Mg-1.8Zn-0.5Zr-xGd alloys derived from the polarization curves

Material	E_s0	$E_s0.5$	$E_s1.0$	$E_s1.5$	$E_s2.0$	$E_s2.5$
E_{corr} , Vvs.SCE	-1.408 ± 0.013	-1.329 ± 0.014	-1.281 ± 0.011	-1.276 ± 0.013	-1.291 ± 0.014	-1.312 ± 0.013
I_{corr} , $\mu A/cm^2$	3.401 ± 0.012	2.614 ± 0.013	2.482 ± 0.011	2.480 ± 0.012	2.485 ± 0.013	2.221 ± 0.013
P_i , mm/y	0.154 ± 0.007	0.127 ± 0.008	0.088 ± 0.007	0.086 ± 0.007	0.091 ± 0.008	0.112 ± 0.008

products are mainly composed of O, Mg, P, Ca, Gd and Zn elements. When the immersion time exceeds 32 h, signals of Gd and Zn in the EDS spectra of corrosion products (C, D and E areas) disappear, while the main elements in the corrosion

layer are detected to be O, Mg, P and Ca. At the same time, it can also be noted that there is only a slight difference of compositions at the white corrosion product (D) and the dense black corrosion product (E) in Fig. 9(d).

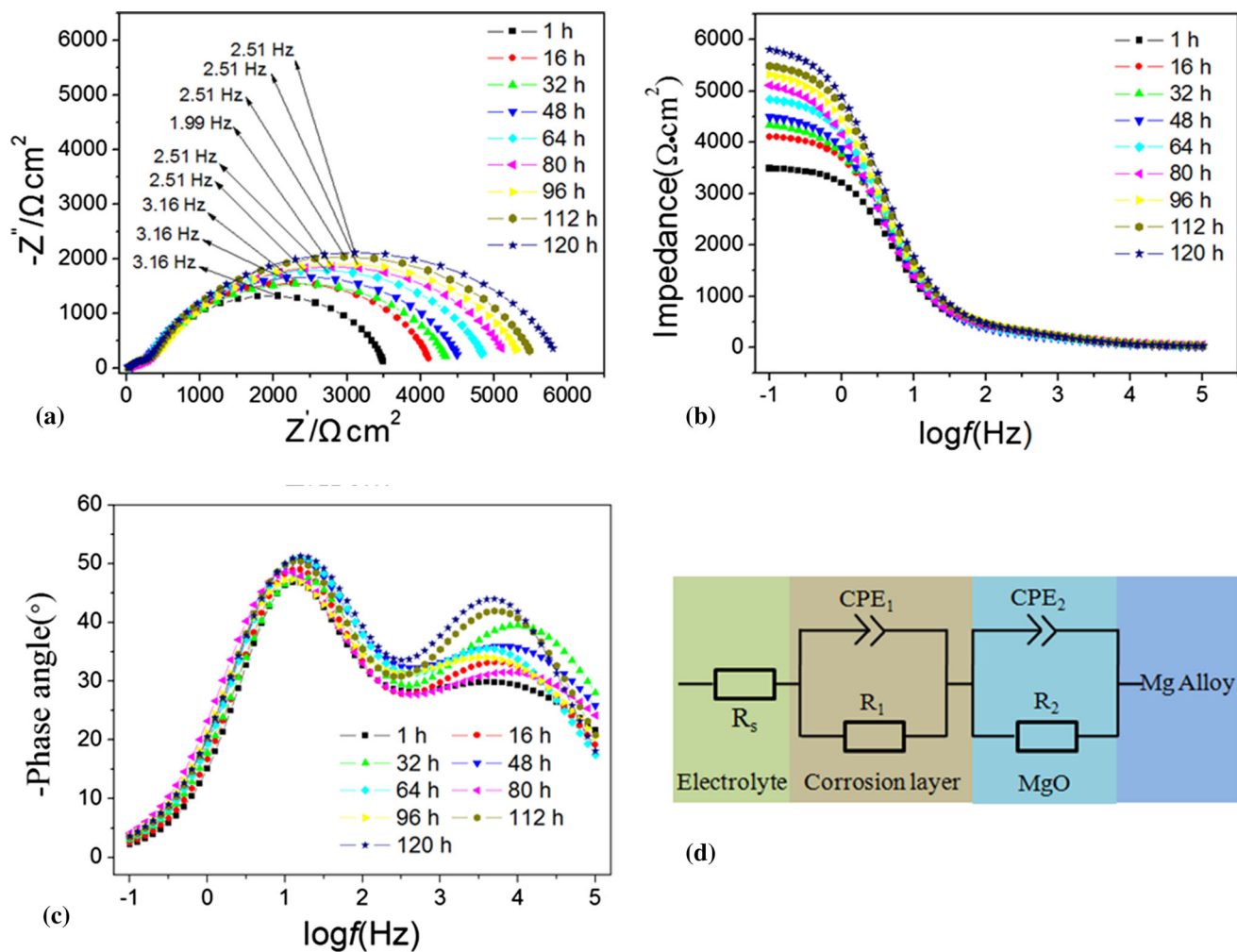


Fig. 7 (a) Nyquist plots, (b) impedance vs. frequency and (c) phase angle vs. frequency plots obtained from the EIS measurements for $E_s1.5$ alloy after different immersion times. (d) Equivalent circuit of the EIS spectra of $E_s1.5$ alloy

Table 3 Values obtained from the EIS spectra of $E_s1.5$ alloy after different immersion time in SBF solution

Time, h	R_s, Ω	$R_1, k\Omega \cdot cm^2$	$CPE_1, \Omega^{-1} \cdot cm^{-2} \cdot s^{-n}$	n_1	$R_2, \Omega \cdot cm^2$	$CPE_2, \Omega^{-1} \cdot cm^{-2} \cdot s^{-n}$	n_2
1	25.2	3.06	20.8	0.896	434	31.9	0.491
16	26.2	3.79	19.4	0.872	335	17.6	0.614
32	17.4	4.10	21.9	0.822	303	21.6	0.636
48	18.6	4.25	21.6	0.845	308	32.2	0.563
64	28.2	4.61	20.0	0.841	319	26.1	0.632
80	23.1	4.84	25.3	0.832	372	33.2	0.524
96	28.8	4.95	22.1	0.834	405	28.5	0.554
112	23.6	5.22	18.7	0.844	418	17.8	0.692
120	23.1	5.63	18.6	0.821	386	16.3	0.732

XPS spectra were acquired for the Mg 1s and Ca 2p regions after SBF immersion for different times. As shown in Fig. 10(a), the alloy surface is composed of Mg and MgO before SBF immersion, as determined by the Mg 1s binding energies at 1303.9 and 1306.3 eV, respectively (Ref 35). After 16 h of immersion, the Mg 1s spectra show the presence of Mg(OH)₂ and MgO. An emerging peak at 1309.4 eV, corresponding to Mg 1s in the (Ca, Mg)₃(PO₄)₂ (Ref 36), can be seen which can be ascribed to attaching, absorbing or

reaction of the SBF with the alloy's metallic surface. Such a phosphate becomes dominating after 48 h of immersion. After 120 h of immersion, the corrosion product is composed of Mg(OH)₂, MgO, (Ca,Mg)₃(PO₄)₂ as well as a small portion of Mg metal which is mostly due to XPS probing depth and peeling off of corrosion product (Ref 37).

Figure 10(b) shows the Ca 2p XPS spectra, in which the calcium compounds are seen to form gradually on the $E_s1.5$ surface. The calcium attachment onto the surface is rather weak

after 16 h of immersion, as evidenced by a very low Ca 2p spectra compared with the Mg KLL Auger spectra arisen from the Mg. However, after longer immersion, the overall Ca content increases as denoted from the XPS intensities. The $\text{Ca}_{10}(\text{PO}_4)_6(\text{OH})_2$ is formed along with the $(\text{Ca},\text{Mg})_3(\text{PO}_4)_2$, as shown in Ca-48h and Ca-120h spectra. Taking the Mg Auger as the reference, the surface content of $\text{Ca}_{10}(\text{PO}_4)_6(\text{OH})_2$ increases

with the immersion time and against the Mg content. It is worth mentioning that the $\text{Ca}_{10}(\text{PO}_4)_6(\text{OH})_2$ is the well-known key composite of the dental enamel and dentin, whose presence indicates a good biocompatibility of the alloy.

4. Discussions

4.1 Effect of Gd Alloying on Microstructure Evolution and Mechanical Properties

The grain size of DRXed magnesium alloys during hot-extrusion depends on the chemical composition, distribution

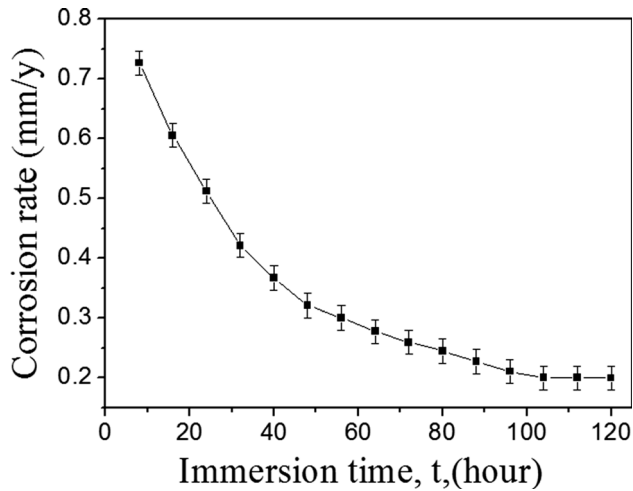


Fig. 8 P_w for $E_s1.5$ alloy immersed in SBF solution for 120 h

Table 4 EDS analyses (as marked in Fig. 9) of $E_s1.5$ alloy after different immersion time in SBF solution

Position	Mass fraction, %					
	O	Mg	P	Ca	Gd	Zn
A	40.02	18.47	16.72	16.52	1.21	1.06
B	42.05	10.84	22.41	2.41	0.92	0.38
C	25.42	46.91	14.86	12.81	0	0
D	52.26	4.84	17.55	25.35	0	0
E	37.56	6.49	24.09	31.86	0	0

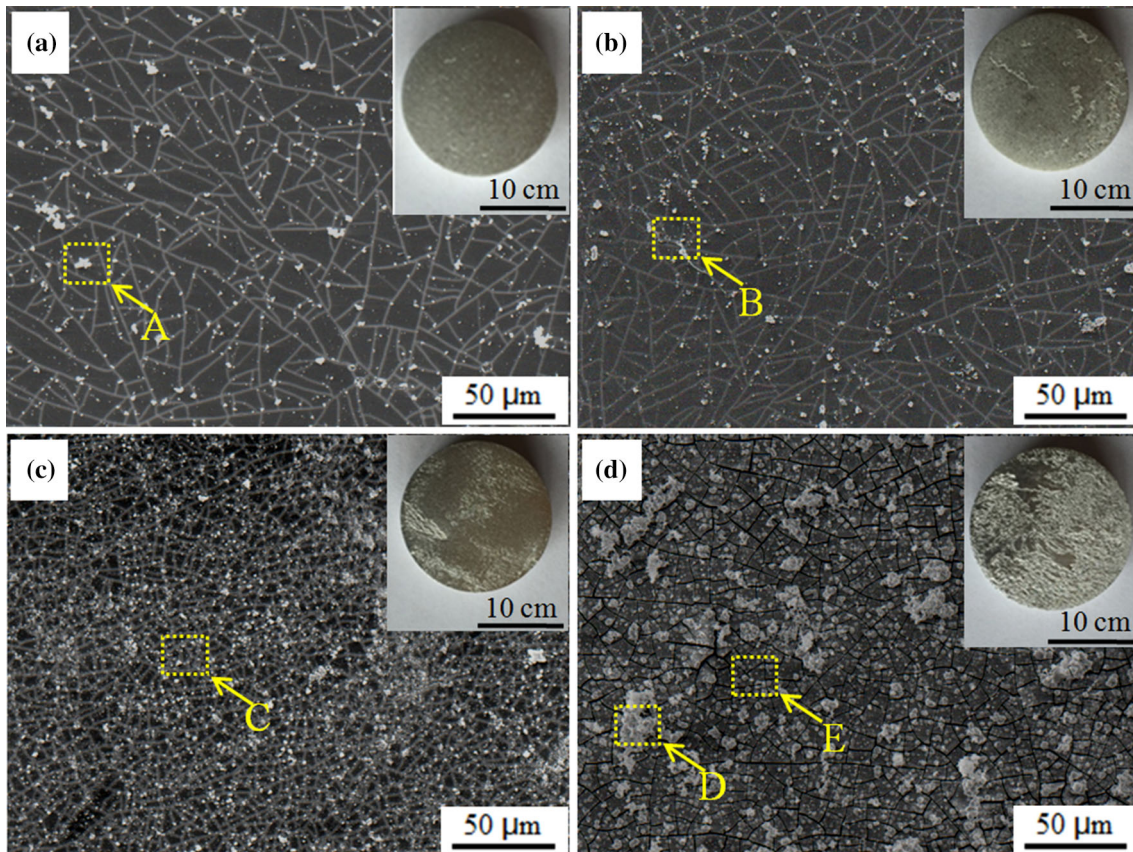


Fig. 9 SEM images of $E_s1.5$ alloy surfaces after immersion in SBF solution for: (a) 16 h; (b) 32 h; (c) 48 h; (d) 120 h. The inset images are optical images of the surfaces after removing corrosion products

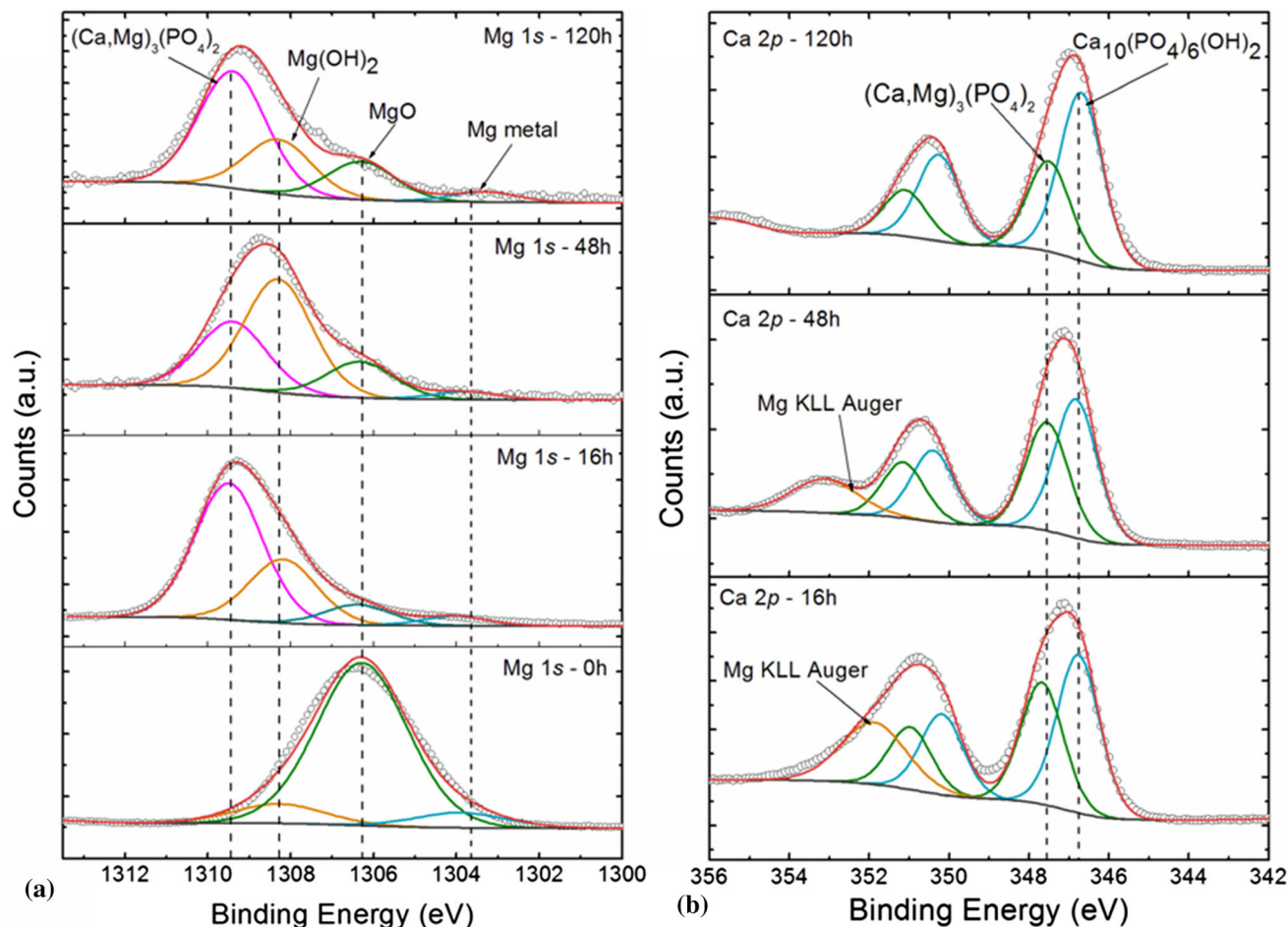


Fig. 10 (a) Mg 1s and (b) Ca 2p XPS spectra of the E₅1.5 alloy recorded after different immersion times in SBF solution

and size of the second-phase particles with the alloy (Ref 38). As shown in Fig. 1, the grains are remarkably refined by Gd alloying. Comparison of the distribution and size of second-phase particles, particularly the (Mg, Zn)₃Gd phase shown in Fig. 2 and 3, indicates that the solubility of Gd in the Mg-1.8Zn-0.5Zr alloy matrix is about 1.5 wt.% at the applied solid solution treatment temperature. Gd solutes can effectively reduce the stacking fault energy of Mg alloys (Ref 39). The smaller the stacking fault energy is, the higher stored energy can be during plastic deformation (Ref 40). The high stored energy by Gd alloying could promote the nucleation rate and the number of nuclei to accelerate DRX (Ref 41). Therefore, it can be considered that Gd dissolved into the matrix plays a major role in the grain refinement process when Gd content is less than 1.5 wt.%. With a Gd content higher than 1.5wt.%, fine second phase particles precipitated out and large particles break during extrusion (Fig. 3). These particles have a pinning effect to the migration of grain boundaries, thus to hinder the grain growth during DRX (Ref 42). Grain refinement has been achieved by combined action of second-phase particles and Gd dissolved into the matrix. Consequently, a significant improvement of mechanical property is obtained, which can be explained by the Hall-Petch equation (Ref 43). The increasing amount of Gd solutes also contributes to improved strengths YS for E₅0.5-1.5 alloys (Fig. 4 and Table 1), namely solid solution strengthening (Ref 44). Meanwhile, Gd dissolved in the alloy matrix can activate more non-basal slip systems

during extrusion (Ref 45). These non-basal slip systems promote the formation of mobile dislocations, thus reducing work hardening in Mg alloys (Ref 46). Additionally, the refined grains also lead to limited stress concentration and twinning formation (Ref 47), thereby improving the plasticity of Gd containing alloy. Moreover, the weaker basal texture components in the extruded alloys make the grains easier to undergo coordinated deformation, which also has a positive effect on the plasticity of Gd alloyed Mg alloys (Ref 48).

Nanoscale precipitates that have a coherent interfacial relationship with the alloy matrix hinder the movement of dislocations during the tensile process to improve the mechanical properties (Ref 49-52). Additionally, the finely broken second phase particle can contribute to the pinning of dislocation movement to a certain extent to improve the alloy strength. These are evidenced by the transition to more ductile fracture (Fig. 5) and increasing UTS, YS and EL with increasing Gd content until 2.0 wt.%.

When the Gd content equals 2.5 wt.%, non-dissolved and retained (Mg, Zn)₃Gd break into micron-sized rod-like particles (~2 μm) in the alloy. These particles usually have a non-coherent interface with the alloy matrix, meaning a weak atomic bonding force with the alloy matrix (Ref 53). During the tensile process, the particles usually become the source of crack initiation and propagation channels (Ref 54), which accelerates the fracture and reduces the mechanical properties of the 2.5 wt.% Gd containing alloy.

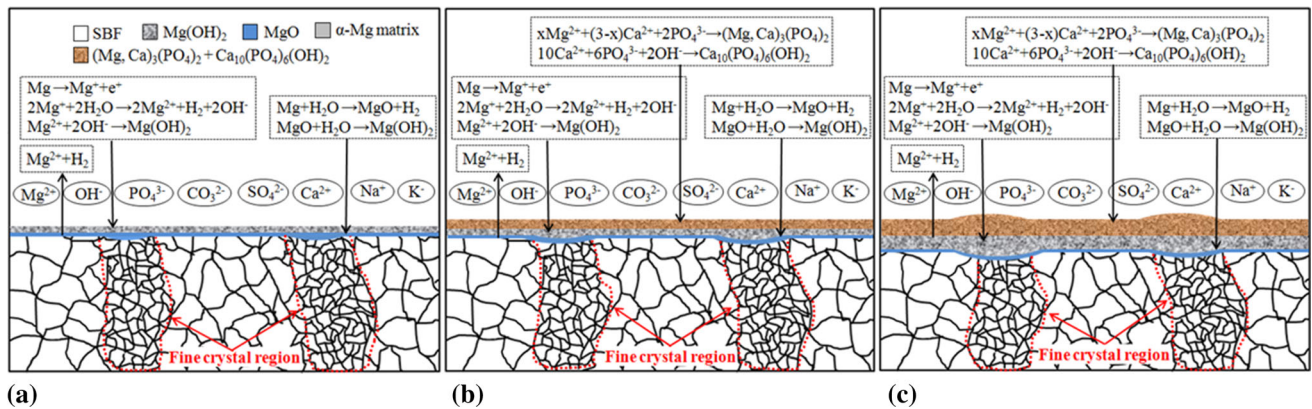


Fig. 11 The corrosion process of $E_s1.5$ alloy in SBF solution: (a) first stage; (b) second stage; (c) third stage

To sum up, the grain size of $E_s0.5 \sim E_s2.5$ alloys is finer than that of E_s0 , which is ascribed to the existence of Gd solutes and second phase particles. Therefore, the YS of $E_s0.5 \sim E_s2.5$ alloys can be improved, within 19 MPa considering solely the contribution from grain refinement. Gd mainly exists in the Mg matrix as solutes in $E_s0.5 \sim E_s1.5$ alloys. Consequently, the increased YS is dominated by the solid solution strengthening mechanism. Continuously increase of YS in $E_s2.0$ is a result of the combination of Gd solutes and Gd-related second phase particles. Nonetheless, the presence of coarse incoherent second phase particles in the $E_s2.5$ alloy leads to the microstructure that is prone to microcracking. Hence, a decrease in YS of $E_s2.5$ is observed.

4.2 Influence of Gd Alloying on Corrosion Behavior

It has been reported that the Gd solutes in Mg alloys can promote the formation of a dense oxide protective film on the surface, which can reduce the cathodic current density and improve the corrosion resistance of the alloy (Ref 55, 56). We found that as the Gd content increases (< 1.5 wt.%), the E_{corr} of the alloy gradually moves positively, meaning the corrosion resistance of the alloy is enhanced. Meanwhile, grain refinement has also been reported to improve corrosion resistance of the alloy (Ref 57). With increasing Gd, the grain size decreases, and the corrosion resistance increases. The enhanced corrosion resistance can be due to that the finer the grains, the more conducive to the formation of a dense and continuous oxide protective film on the alloy surface. Meanwhile, the refined grain structure can also reduce the discontinuity between the oxide protective film and the alloy (Ref 58). Hence, the oxide protective film can effectively prevent the corrosive medium from penetrating into the alloy matrix.

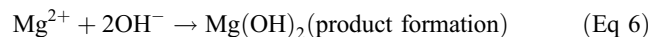
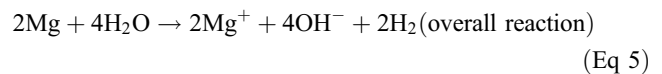
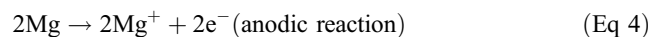
When the Gd content is greater than 1.5 wt.%, the grain size decreases slowly, and the number and size of the second-phase particles in the alloy increase with increasing Gd. These second-phase particles usually act as the cathode and cause galvanic corrosion to the surrounding α -Mg matrix. Increasing size of second-phase particles increases the power of galvanic corrosion with the surrounding α -Mg matrix, accelerates the dissolution of the matrix, and therefore reduces the corrosion resistance of the alloy. Meanwhile, the second-phase particles can be peeled off from the matrix, resulting in large active areas to corrode (Ref 59). This leads to an increase in the corrosion

rate. Therefore, a gradual decrease in the corrosion resistance of the alloy when the Gd content is in the range of 1.5-2.5 wt.%.

4.3 Corrosion Mechanism

It is noteworthy that the corrosion of Mg is a complex process and different mechanisms have been proposed (Ref 60, 61). In the $E_s1.5$ alloy, fine DRX grains containing subgrains are clustered and distributed along the ED (Fig. 1 d). In Mg alloys, these areas that contain high-density dislocations are usually acted as anodes during corrosion and preferentially corrode (Ref 62). Therefore, as the immersion time increases, the number and width of the strip-shaped corrosion zone on the alloy surface gradually increase. The immersion, electrochemical and surface analysis demonstrate that the corrosion resistance of the $E_s1.5$ alloy is the best among the other alloys, which is due to the grain refinement and the formation of fine second-phase particles. The corrosion mechanism of the $E_s1.5$ alloy in the SBF solution is schematically summarized in Fig. 11. The corrosion process undergoes three distinct stages as follows.

Stage 1 Hydroxidation (0-48 h), Fig. 11(a): chemical reactions between the Mg matrix and water dominates. The corrosion of $E_s1.5$ alloy in SBF occurs through the following partial reactions:

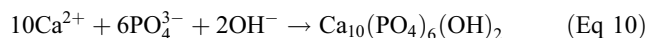
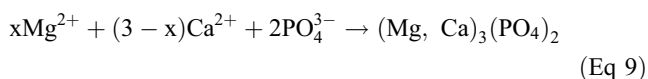


The corrosion product layer of $Mg(OH)_2$ was gradually thickened with immersion time, and the alloy surface exposed to SBF gradually decreased. As a result, R_{p1} and R_{p2} in EIS rapidly increased, and corrosion rate declined rapidly. The corrosion layer became thicker with time and inhibited the penetration of SBF solution into the matrix. Therefore, the reaction that involves the fresh-produced and native MgO layers is also possible:



Side reactions at this stage may also happen through, e.g., $x\text{Mg}^{2+} + (3-x)\text{Ca}^{2+} + 2\text{PO}_4^{3-}$ to form a certain amount of $(\text{Mg}, \text{Ca})_3(\text{PO}_4)_2$. However, the Ca attachment to the matrix is rather low as shown in Fig. 10(b), leading to relative smaller reaction rates compared to hydroxidation.

Stage 2 Phosphatization and hydroxidation (48-96 h), Fig. 11(b). The thickness of $\text{Mg}(\text{OH})_2$ corrosion layer and the concentration of Mg^{2+} in SBF solution increase gradually. A compact mixture of $\text{Mg}(\text{OH})_2$, $(\text{Ca}, \text{Mg})_3(\text{PO}_4)_2$ and $\text{Ca}_{10}(\text{PO}_4)_6(\text{OH})_2$ corrosion products has formed, as verified by the EDS (Fig. 9) and XPS (Fig. 10). With increasing immersion time, the continuous thickening of the corrosion layer led to the increase in R_{p1} and R_{p2} . Therefore, the corrosion rate of the alloy decreased, which was beneficial to the overflow of the generated H_2 through the corrosion layer (Ref 63, 64). The reactions are as follows:



Stage 3 Equilibrium (96-120 h), Fig. 11(c). During the renewal cycles of the SBF solution, the formation and dissolution of corrosion products reached a dynamic equilibrium, resulting in small changes in R_{p1} and R_{p2} . The alloy surface is covered by the MgO , $\text{Mg}(\text{OH})_2$, $(\text{Ca}, \text{Mg})_3(\text{PO}_4)_2$ compounds as well as a bio-preferable $\text{Ca}_{10}(\text{PO}_4)_6(\text{OH})_2$.

5. Conclusions

In conclusion, we systematically studied the effects of Gd alloying on the microstructure, mechanical properties, and corrosion resistance of as-extruded Mg-1.8Zn-0.5Zr alloys with prior solid solution treatment. The main conclusions are as follows:

1. The grains of the extruded Mg-1.8Zn-0.5Zr-xGd alloy are significantly refined by the Gd alloying. When Gd content is 1.5 wt.%, nanoscale $(\text{Mg}, \text{Zn})_3\text{Gd}$ and $\text{Mg}_2\text{Zn}_{11}$ phases are precipitated in the alloy, and the volume fraction and size of the second phase gradually increase with the increase in Gd content. When Gd content is 2.5 wt.%, a large number of micron-level $(\text{Mg}, \text{Zn})_3\text{Gd}$ phase appear in the alloy.
2. Under the combined action of fine grain strengthening, solution strengthening and second-phase strengthening, the mechanical properties of the alloy gradually increase with Gd content below 2.0 wt.%. When Gd content is higher than 2.0 wt.%, a large number of micron-level second phase appear, resulting in decreased mechanical properties of the alloy. The alloy with 2.0 wt.% Gd has the best mechanical properties: UTS of 288.5 MPa, YS of 257.6 MPa and EL of 33.5%.
3. The refined grains of the alloys by Gd alloying result in increasing corrosion resistance as the Gd content in-

creases to 1.5 wt.%. For Gd content greater than 1.5 wt.%, the increase in the size and number of the second-phase particles causes the corrosion resistance of the alloy to decrease. The E_s1.5 alloy, i.e., the alloy with 1.5 wt.% Gd, has the best corrosion resistance.

4. The corrosion process can be divided into three stages: Stage 1, the rapid increase in $\text{Mg}(\text{OH})_2$ on the surface leads to a rapid decrease in the corrosion rate; Stage 2, the dense $\text{Mg}(\text{OH})_2$, $(\text{Ca}, \text{Mg})_3(\text{PO}_4)_2$, $\text{Ca}_{10}(\text{PO}_4)_6(\text{OH})_2$ corrosion layer leads to a slow decrease in the corrosion rate; Stage 3, the formation and dissolution of corrosion products reach a dynamic equilibrium and the corrosion rate becomes stable.

Acknowledgments

This work was financially supported by the Education Department of Henan Province (20A430010), National Natural Science Foundation of China (U1804146, 52111530068), Foreign Experts and Introduction Project of Henan Province (HNGD2020009) and Academy of Finland Grant #311934. The Center for Material Analysis, University of Oulu, Finland, is acknowledged for XPS measurements.

Conflict of interest

The authors declare no conflict of interest.

References

1. Y.X. Liu, M. Curioni, and Z. Liu, Correlation between Electrochemical Impedance Measurements and Corrosion Rates of Mg-1Ca Alloy in Simulated Body Fluid, *Electrochim. Acta.*, 2018, **264**, p 101–108.
2. D. Mareci, G. Bolat, J. Izquierdo, C. Crimu, C. Munteanu, I. Antoniac, and R.M. Souto, Electrochemical Characteristics of Bioresorbable Binary MgCa Alloys in Ringer's Solution: Revealing the Impact of Local pH Distributions during In-Vitro Dissolution, *Mater. Sci. Eng. C*, 2016, **60**, p 402–410.
3. Y.J. Chen, Z.G. Xu, C. Smith, and J. Sankar, Recent Advances on the Development of Magnesium Alloys for Biodegradable Implants, *Acta Biomater.*, 2014, **10**, p 4561–4573.
4. Y.C. Wan, S.Y. Xu, C.M. Liu, Y.H. Gao, S.N. Jiang, and Z.Y. Chen, Enhanced Strength and Corrosion Resistance of Mg-Gd-Y-Zr Alloy with Ultrafine Grains, *Mater. Lett.*, 2018, **213**, p 274–277.
5. X.N. Gu, Y.F. Zheng, S.P. Zhong, T.F. Xi, J.Q. Wang, and W.H. Wang, Corrosion of, and Cellular Responses to Mg-Zn-Ca Bulk Metallic Glasses, *Biomaterials*, 2010, **31**, p 1093–1103.
6. R.C. Zeng, W. Ke, Y.B. Xu, E.H. Han, and Z.Y. Zhu, Recent Development and Application of Magnesium Alloys, *Acta Metall. Sin.*, 2001, **37**, p 673–685.
7. X.N. Gu, N. Li, Y.F. Zheng, and L.Q. Ruan, In Vitro Degradation Performance and Biological Response of a Mg-Zn-Zr Alloy, *Mater. Sci. Eng. B*, 2011, **176**, p 1778–1784.
8. X.B. Zhang, Z.X. Ba, Q. Wang, Y.J. Wu, Z.Z. Wang, and Q. Wang, Uniform Corrosion Behavior of GZ51K Alloy with Long Period Stacking Ordered Structure for Biomedical Application, *Corros. Sci.*, 2014, **88**, p 1–5.
9. Z.Q. Zhang, X. Liu, W.Y. Hu, J.H. Li, Q.C. Le, L. Bao, Z.J. Zhu, and J.Z. Cui, Microstructures, Mechanical Properties and Corrosion Behaviors of Mg-Y-Zn-Zr Alloys with Specific Y/Zn Mole Ratios, *J. Alloys. Compd.*, 2015, **624**, p 116–125.
10. J.Y. Zhang, Z.X. Kang, and L.L. Zhou, Microstructure Evolution and Mechanical Properties of Mg-Gd-Nd-Zn-Zr Alloy Processed by Equal Channel Angular Processing, *Mater. Sci. Eng. A*, 2015, **647**, p 184–190.
11. S. Gollapudi, Grain Size Distribution Effects on the Corrosion Behaviour of Materials, *Corros. Sci.*, 2012, **62**, p 90–94.

12. X.B. Zhang, Z.X. Ba, Z.Z. Wang, Y.J. Wu, and Y.J. Xue, Effect of LPSO Structure on Mechanical Properties and Corrosion Behavior of As-Extruded GZ51K Magnesium Alloy, *Mater. Lett.*, 2016, **163**, p 250–253.
13. F.Y. Cao, Z.M. Shi, G.L. Song, M. Liu, M.S. Dargusch, and A. Atrens, Influence of Hot Rolling on the Corrosion Behavior of Several Mg-X Alloys, *Corros. Sci.*, 2015, **90**, p 176–191.
14. K. Liu, J.H. Zhang, L.L. Rokhlin, F.M. Elkin, D.X. Tang, and J. Meng, Microstructures and Mechanical Properties of Extruded Mg-8Gd-0.4Zr Alloys Containing Zn, *Mater. Sci. Eng. A*, 2009, **505**, p 13–19.
15. X.B. Zhang, G.Y. Yuan, L. Mao, J.L. Niu, and W.J. Ding, Biocorrosion Properties of as-Extruded Mg-Nd-Zn-Zr Alloy Compared with Commercial AZ31 and WE43 Alloys, *Mater. Lett.*, 2012, **66**, p 209–211.
16. H. Yao, J.B. Wen, Y. Xiong, Y. Lu, and M. Huttula, Microstructure Evolution in Mg-Zn-Zr-Gd Biodegradable Alloy: The Decisive Bridge Between Extrusion Temperature and Performance, *Front. Chem.*, 2018, **6**, p 71.
17. H. Huang, G.Y. Yuan, C.L. Chen, W.J. Ding, and Z.C. Wang, Excellent Mechanical Properties of an Ultrafine Grained Quasicrystalline Strengthened Magnesium Alloy with Multi-Modal Microstructure, *Mater. Lett.*, 2013, **107**, p 181–184.
18. S.D. Wang, D.K. Xu, X.B. Chen, E.H. Han, and C. Dong, Effect of Heat Treatment on the corrosion resistance and mechanical properties of an as-forged Mg-Zn-Y-Zr alloy, *Corros. Sci.*, 2015, **92**, p 228–236.
19. H.W. Miao, H. Huang, Y.J. Shi, H. Zhang, J. Pei, and G.Y. Yuan, Effects of Solution Treatment before Extrusion on the Microstructure, Mechanical Properties and Corrosion of Mg-Zn-Gd Alloy in Vitro, *Corros. Sci.*, 2017, **122**, p 90–99.
20. J.M. Seitz, A. Lucas, and M. Kirschenr, Magnesium-Based Compression Screws: A Novelty in the Clinical use of Implants, *Jom.*, 2016, **68**, p 1177–1181.
21. J.C. Bousquet, S. Sanini, D.D. Stark, P.F. Hahn, M. Nigam, J. Wittmann, and J.T. Ferrucci, Gd-Dota: Characterization of a New Paramagnetic Complex, *Radiology*, 1988, **166**, p 693–698.
22. H. Yao, B.Y. Fang, H.N. Shi, H. Singh, M. Huttula, and W. Cao, Microstructures, Mechanical Properties and Degradation Behavior of As-Extruded Mg-1.8Zn-0.5Zr-xGd ($0 \leq x \leq 2.5$ wt.%) Biodegradable Alloys, *J. Mater. Sci.*, 2021, **56**, p 11137–11153.
23. H. Yao, J.B. Wen, Y. Xiong, Y. Liu, Y. Lu, and W. Cao, Microstructures, Mechanical Properties and Corrosion Behavior of As-Cast Mg-2.0Zn-0.5Zr-xGd (wt.%) Biodegradable Alloys, *Materials*, 2018, **11**, p 1564.
24. H. Yao, J.B. Wen, Y. Xiong, Y. Lu, F.Z. Ren, and W. Cao, Extrusion Temperature Impacts on Biometallic Mg-2.0Zn-0.5Zr-3.0Gd (wt.%) Solid-Solution Alloy, *J. Alloys. Compd.*, 2018, **739**, p 468–480.
25. M. Ascencio, M. Pekguleryuz, and S. Omanovic, An Investigation of the Corrosion Mechanisms of WE43 Mg Alloy in a Modified Simulated Body Fluid Solution: The Effect of Electrolyte Renewal, *Corros. Sci.*, 2015, **91**, p 297–310.
26. J.L. Li, L.L. Tan, P. Wan, X.M. Yu, and K. Yang, Study on Microstructure and Properties of Extruded Mg-2Nd-0.2Zn Alloy as Potential Biodegradable Implant Material, *Mater. Sci. Eng. C*, 2015, **49**, p 422–429.
27. J. Liu, L.X. Yang, C.Y. Zhang, B. Zhang, T. Zhang, Y. Li, K.M. Wu, and F.H. Wang, Role of the LPSO Structure in the Improvement of Corrosion Resistance of Mg-Gd-Zn-Zr Alloys, *J. Alloys. Compd.*, 2019, **782**, p 648–658.
28. J.A. Österreicher, M. Kumar, A. Schiffl, S. Schwarz, and G.R. Bourret, Secondary Precipitation during Homogenization of Al-Mg-Si Alloys: Influence on High Temperature Flow Stress, *Mater. Sci. Eng. C*, 2017, **687**, p 175–180.
29. L.L. Wei and L. Chang, Structure of Coherent Mg₂TiO₄ Oxide Formed Between TiN and MgO, *Mater. Lett.*, 2018, **213**, p 227–230.
30. B. Homayun and A. Afshar, Microstructure, Mechanical Properties, Corrosion Behavior and Cytotoxicity of Mg-Zn-Al-Ca Alloys as Biodegradable Materials, *J. Alloys. Compd.*, 2014, **607**, p 1–10.
31. G.L. Song and Z.Q. Xu, The Surface, Microstructure and Corrosion of Magnesium Alloy AZ31 Sheet, *Electrochim. Acta.*, 2010, **55**, p 4148–4161.
32. J.B. Jorcin, M.E. Orazem, N. Pébère, and B. Tribollet, CPE Analysis by Local Electrochemical Impedance Spectroscopy, *Electrochim. Acta.*, 2006, **51**, p 1473–1479.
33. M.I. James, G.S. Wu, Y. Zhao, D.R. McKenzie, M.M.M. Bilek, and P.K. Chu, Electrochemical Corrosion Behavior of Biodegradable Mg-Y-RE and Mg-Zn-Zr Alloys in Ringer's Solution and Simulated Body Fluid, *Corros. Sci.*, 2015, **91**, p 160–184.
34. W.H. Ma, Y.J. Liu, W. Wang, and Y.Z. Zhang, Effects of Electrolyte Component in Simulated Body Fluid on the Corrosion Behavior and Mechanical Integrity of Magnesium, *Corros. Sci.*, 2015, **98**, p 201–210.
35. P.J. Burke, Z. Bayindir, and G.J. Kipouros, X-ray Photoelectron Spectroscopy (XPS) Investigation of the Surface Film on Magnesium Powders, *Appl. Spectrosc.*, 2012, **66**, p 510–518.
36. I.J.T. Jensen, A. Thøgersen, O.M. Løvrvik, H. Schreuders, B. Dam, and S. Diplas, X-ray Photoelectron Spectroscopy Investigation of Magnesium Sputtered Mg-Ti-H Thin Films, *Int. J. Hydrogen Energy*, 2013, **38**, p 10704–10715.
37. L. Kuai, E. Kan, W. Cao, M. Huttula, S. Ollikkala, T. Ahopelto, A.P. Honkanen, S. Huotari, W.H. Wang, and B.Y. Geng, Mesoporous LaMnO_{3+δ} Perovskite from Spray - Pyrolysis with Superior Performance for Oxygen Reduction Reaction and Zn - Air Battery, *Nano Energy*, 2018, **43**, p 81–90.
38. K. Huang and R.E. Logé, A Review of Dynamic Recrystallization Phenomena in Metallic Materials, *Mater. Des.*, 2016, **111**, p 548–574.
39. Y.H. Sun, R.C. Wang, J. Ren, C.Q. Peng, and Z.Y. Cai, Microstructure, Texture, and Mechanical Properties of As-Extruded Mg-xLi-3Al-2Zn-0.2Zr alloys (x=5, 7, 8, 9, 11 wt.%), *Mater. Sci. Eng. A*, 2019, **755**, p 201–210.
40. H. Esmaeilpour, A. Zarei-Hanzaki, N. Eftekhari, H.R. Abedi, and M.R. Ghandehari Ferdowsi, Strain Induced Transformation, Dynamic Recrystallization and Texture Evolution During Hot Compression of an Extruded Mg-Gd-Y-Zn-Zr alloy, *Mater. Sci. Eng. A*, 2020, **778**, p 139021.
41. B.B. Dong, Z.M. Zhang, J.M. Yu, X. Che, M. Meng, and J.L. Zhang, Microstructure, Texture Evolution and Mechanical Properties of Multidirectional Forged Mg-13Gd-4Y-2Zn-0.5Zr Alloy Under Decreasing Temperature, *J. Alloys. Compd.*, 2020, **823**, p 153776.
42. J. Luo, H. Yan, R.S. Chen, and E.H. Han, Effects of Gd Concentration on Microstructure, Texture and Tensile Properties of Mg-Zn-Gd Alloys Subjected to Large Strain Hot Rolling, *Mater. Sci. Eng. A*, 2014, **614**, p 88–95.
43. Y.F. Wang, F. Zhang, Y.T. Wang, Y.B. Duan, K.J. Wang, W.J. Zhang, and J. Hu, Effect of Zn Content on the Microstructure and Mechanical Properties of Mg-Gd-Y-Zr Alloys, *Mater. Sci. Eng. A*, 2019, **745**, p 149–158.
44. L. Xiao, G.Y. Yang, Y. Liu, S.F. Luo, and W.Q. Jie, Microstructure Evolution, Mechanical Properties and Diffusion Behaviour of Mg-6Zn-2Gd-0.5Zr Alloy During Homegenization, *J. Mater. Sci. Technol.*, 2018, **34**, p 2246–2255.
45. G.S. Zhang, Y.Z. Meng, F.F. Yan, Z. Gao, Z.M. Yan, and Z.M. Zhang, Microstructure and Texture Evolution of Mg-RE-Zn Alloy Prepared by Repetitive Upsetting-Extrusion under Different Decreasing Temperature Degrees, *J. Alloys. Compd.*, 2020, **815**, p 152452.
46. X.Y. Qian, Y. Zeng, B. Jiang, Q.R. Yang, Y.J. Wang, G.F. Quan, and F.S. Pan, Grain Refinement Mechanism and Improved Mechanical Properties in Mg-Sn Alloy with Trace Y Addition, *J. Alloys. Compd.*, 2020, **820**, p 153122.
47. H.F. Sun, C.J. Li, and W.B. Fang, Evolution of Microstructure and Mechanical Properties of Mg-3.0Zn-0.2Ca-0.5Y Alloy by Extrusion at Various Temperatures, *J. Mater. Process. Technol.*, 2016, **229**, p 633–640.
48. Q.G. Jia, W.X. Zhang, Y. Sun, C.X. Xu, J.S. Zhang, and J. Kuan, Microstructure and Mechanical Properties of As-Cast and Extruded Biomedical Mg-Zn-Y-Zr-Ca Alloy at Different Temperatures, *Trans. Nonferrous Met. Soc. China*, 2019, **29**, p 515–525.
49. L. Li, Y. Wang, C.C. Zhang, T. Wang, and H. Lv, Effect of Yb Concentration on Recrystallization, Texture and Tensile Properties of Extruded ZK60 Magnesium Alloys, *Mater. Sci. Eng. A*, 2020, **788**, p 139609.
50. Y.Z. Du, X.G. Qiao, M.Y. Zheng, K. Wu, and S.W. Xu, The Microstructure, Texture and Mechanical Properties of Extruded Mg-5.3Zn-0.2Ca-0.5Ce (wt.%) Alloy, *Mater. Sci. Eng. A*, 2015, **620**, p 164–171.
51. Q.M. Peng, B.C. Ge, H. Fu, Y. Sun, Q. Zu, and J.Y. Huang, Nanoscale Coherent Interface Strengthening of Mg Alloys, *Nanoscale*, 2018, **10**, p 18028.
52. Z.Y. Zhao, P.K. Bai, R.G. Guan, V. Murugadoss, H. Liu, X.J. Wang, and Z.H. Guo, Microstructural Evolution and Mechanical Strengthen-

- ing Mechanism of Mg-3Sn-1Mn-1La Alloy After Heat Treatments, *Mater. Sci. Eng. A*, 2018, **734**, p 200–209.
53. D.H. Bae, S.H. Kim, D.H. Kim, and W.T. Kim, Deformation Behavior of Mg-Zn-Y Alloys Reinforced by Icosahedral Quasicrystalline Particles, *Acta. Mater.*, 2002, **50**, p 2343–2356.
 54. H.Y. Yu, H.G. Yan, J.H. Chen, B. Su, Y. Zheng, Y.J. Shen, and Z.J. Ma, Effect of Minor Gd Addition on Microstructures and Mechanical Properties of the High Strain-Rate Rolled Mg-Zn-Zr Alloys, *J. Alloys. Compd.*, 2014, **586**, p 757–765.
 55. S.Q. Yin, W.C. Duan, W.H. Liu, L. Wu, J.M. Yu, Z.L. Zhao, M. Liu, P. Wang, J.Z. Cui, and Z.Q. Zhang, Influence of Specific Second Phases on Corrosion Behaviors of Mg-Zn-Gd-Zr Alloys, *Corros. Sci.*, 2020, **166**, p 108419.
 56. N. Hort, Y. Huang, D. Fechner, M. Störmer, C. Blawert, F. Witte, C. Vogt, H. Drücker, R. Willumeit, K.U. Kainer, and F. Feyerabend, Magnesium Alloys as Implant Materials – Principles of Property Design for Mg-RE Alloys, *Acta. Biomater.*, 2010, **6**, p 1714–1725.
 57. G.R. Argade, S.K. Panigrahi, and R.S. Mishra, Effects of Grain Size on the Corrosion Resistance of Wrought Magnesium Alloys Containing Neodymium, *Corros. Sci.*, 2012, **58**, p 145–151.
 58. Y.L. Zhou, Y.C. Li, D.M. Luo, Y.F. Ding, and P. Hodgson, Microstructures, Mechanical and Corrosion Properties and Biocompatibility of as Extruded Mg-Mn-Zn-Nd Alloys for Biomedical Applications, *Mater. Sci. Eng. C*, 2015, **49**, p 93–100.
 59. A. Srinivasan, Y. Huang, C.L. Mendis, C. Blawert, K.U. Kainer, and N. Hort, Investigation on Microstructures, Mechanical and Corrosion Properties of Mg-Gd-Zn Alloys, *Mater. Sci. Eng. A*, 2014, **595**, p 224–234.
 60. G.L. Song and A. Atrens, Corrosion Mechanisms of Magnesium Alloys, *Adv. Eng. Mater.*, 1999, **1**, p 11–33.
 61. G.L. Song and A. Atrens, Understanding Magnesium Corrosion: A Framework for Improved Alloy Performance, *Adv. Eng. Mater.*, 2003, **5**, p 837–858.
 62. F.F. Cao, K.K. Deng, K.B. Nie, J.W. Kang, and H.Y. Niu, Microstructure and Corrosion Properties of Mg-4Zn-2Gd-0.5Ca Alloy Influenced by Multidirectional Forging, *J. Alloys. Compd.*, 2019, **770**, p 1208–1220.
 63. L. Yang and E. Zhang, Biocorrosion Behavior of Magnesium Alloy in Different Simulated Fluids for Biomedical Application, *Mater. Sci. Eng. C*, 2009, **29**, p 1691–1696.
 64. W.A. Badawy, N.H. Hilal, M. El-Rabiee, and H. Nady, Electrochemical Behavior of Mg and Some Mg Alloys in Aqueous Solutions of Different pH, *Electrochim. Acta.*, 2010, **55**, p 1880–1887.

Publisher's Note Springer Nature remains neutral with regard to jurisdictional claims in published maps and institutional affiliations.